Stretching Effect on Nafion Fibrillar Nanostructure

Laurent Rubatat[†] and Olivier Diat*[,‡]

UMR SPrAM 5819, (CEA,CNRS, UJF), 38054 Grenoble Cedex 9, France

Received February 12, 2007; Revised Manuscript Received September 28, 2007

ABSTRACT: Drawing experiments have been performed to point out the fibrillar nature of Nafion membranes. The structure evolution upon drawing was monitored by small-angle X-ray scattering and small-angle neutron scattering (SAXS and SANS). The spectra were analyzed within the q-range 0.02−0.5 Å^{-1} corresponding to a length scale larger than the fibril diameter, which is in the order of 4 nm. This q-range includes the so-called ionomer peak, analyzed as the peak of the structure factor and correlated to the average distance between the polymer fibrils. A basic deformation model of a fibrillar system is proposed to simulate the peak evolution. The other scattering feature treated in this paper is the power law of the scattering curve at low q analyzed considering a cylinder form factor, which is consistent with a fibrillar structure.

1. Introduction

Nafion is a widely used membrane for fuel cell applications due to its good chemical, mechanical, and proton-transporting properties. Since its commercialization in the 1960s, much research has been carried out to understand its structure. For an overview of experimental results and models, see references 1−4 for examples. Experiments in the very diluted regime, with volume fraction of polymer $\phi_p < 10\%$, show the existence of elongated aggregates of Nafion polymer with the ionic groups at the surface.[5] In the concentrated regime, $\phi_p > 70\%$, water pools containing the ionic groups within a polytetrafluorethylene matrix were proposed by Gierke.[6] Although the transition between the concentrated and diluted regimes[7] is not yet well understood, recent works propose the existence of elongated polymeric aggregates in the concentrated region which matches the results between both regimes.[8−10] Those aggregates result in a strong attractive interaction between the fluorinated backbones for which the extension of a crystalline organization is limited by the pendant chains[11] and the dipolar interaction between sulfonated groups. SANS, employing the contrast variation method, was used to resolve the shape of the aggregates, which were found to be cylinder-like on first approximation with an averaged diameter of about 4 nm. At a larger length scale, a local orientational order of the elongated aggregates into bundles with a correlation length of the order of 50−100 nm[10,12] is proposed to explain the modulation detected by atomic force microscopy[13,14] as well as the low-q scattering upturn observed on SAXS curves.[10,15] This later excess of scattering signal limits the range of the q^{-1} power law[10,16,17] characteristic of a cylinder form factor and prevents the determination of the full length of the elongated aggregates. In this paper, we propose an analysis of SAXS and SANS results measured on drawn Nafion membranes, using a basic structural model which depicts the local orientation between elongated polymeric aggregates.

Partial orientation of the structure is possible upon drawing, resulting in new film properties.[18,19] Numerous experiments on drawn Nafion have been performed in order to study the effect of deformation on the distribution of the aqueous domains within the polymer matrix and to investigate the water sorption and mechanical properties.[20−23] Plastic and elastic deformation were quantified as a function of preparation process and pretreatment history, with the aim of demonstrating how mechanical constraints can impact fuel cell performance.[6,22−26] Dynamical mechanical experiments permitted the assignment of the α and β relaxations to long-range chain mobility and segmental motion, respectively, which are both dependent on the ionic interactions.[27−30] The contribution of the main chain and the pendant chains to the relaxation, as a function of temperature, can be deconvoluted and related, respectively, to the interaction of the backbones and to the electrostatic interactions. Measurements of proton conductivity on stretched membranes show that conductivity decreases perpendicularly to the drawing axis and increases along this axis.[23,31,32] However, the conductivity evolves after deformation due to polymer creep.[32,33] This latter feature was studied using the birefringence property of Nafion.[33−35] The authors show that the birefringence data analyzed considering bundles of elongated, connected, and entangled polymeric aggregates were in agreement with the nanometer scale morphology probed with scattering techniques.

The majority of experiments on stretched Nafion membranes were performed with the aim of understanding the morphology. For example, Elliott et al.[25] discussed SAXS patterns in terms of the spherical nature of the clusters and suggested, when the Nafion film is stretched, an increase and a decrease in coherence of the intercluster spacings perpendicular and parallel to the draw direction, respectively. The possibility of deformation of the spherical clusters is thus rejected on the basis of their analysis. Alternatively, Londono et al.[22] concluded from their scattering data that water domains in stretched Nafion consist of coalesced water pools, which form cylindrical or lamellar aqueous domains. In previous works,[12,31,33,34] the scattering spectra of Nafion under stretching as well as the Hermann factor variation as a function of the drawing ratio were explained in terms of the orientation of elongated polymeric aggregates.

In this paper, small-angle X-ray and neutron scattering were used to monitor the evolution of the morphology upon deformation, for scattering vector, q, ranging from 0.02 to 0.5 Å^{-1}. This q-range includes the well-known ionomer peak analyzed as the first-order peak of a structure factor and at smaller angles a power-law characteristic of a form factor of elongated scattering objects.

* Corresponding author. E-mail: olivier.diat@cea.fr.
[†] New address: Pau University, UMR IPREM 5254, 64000 Pau, France.
[‡] New address: ICSM, UMR 5257, CEA Marcoule BP 17171, 30207 Bagnols s/ Céze, France.

10.1021/ma070362s CCC: $37.00
Published on Web 11/30/2007

2. Experimental Section

Sample Preparation. Nafion 117 and 125 films were used (Aldrich); the membranes are characterized by their respective equivalent weights (EW) 1100 and 1200 g equiv^{-1} and their respective thicknesses, 175 and 125 μm. The standard procedure was applied for membrane preparation in terms of cleaning; the membranes were soaked twice in HNO_3 (1 M) for 2 h, then washed for 1 h in deionized water. The acid form was used for X-ray experiments. However, for neutron experiments, the tetramethylammonium (TMA^+) neutralized form was used. The neutralized form was obtained by soaking the membranes in a saturated TMA chloride solution for 2 days. The membranes were then rinsed in pure water in order to remove the excess of salt. Nafion membranes were cut in a rectangular shape, 5×15 mm^2, and fixed between two clamps along their length in a homemade drawing cell. With the use of two coupled endless screws, a single membrane was stretched, keeping the symmetry center of the deformation at the beam position. In this paper, membrane deformation is quantified by λ_{def}, defined as $\lambda_{def} = (L - L_0)/L_0$, where L_0 is the initial distance between the clamps and L the distance during the deformation. λ_{def} is expressed in percentage. To highlight some of the stretching features, the Nafion 125 membrane was dry-stretched. The treatment consists of taking a water-swollen membrane tightened between two clamps and then dried in an oven at 100 °C for a couple of hours in order to quench the oriented structure at ambient temperature. The sample used in the micro-SAXS experiment is made by cutting a squared piece 1×1 mm^2 out of the central part of the stretched and quenched membrane, keeping track of the stretching direction (SD).

SANS Experiments. 2D SANS spectra were recorded on the D22 beam line at ILL-Grenoble. The neutron wavelength was 10 Å, and the detector was off centered and located 3 m from the sample position. q is defined as the norm of the scattering vector, $q = 4\pi/\lambda \sin(\theta_{scatt}/2)$, where θ_{scatt} is the scattering angle. Spectra were recorded before and after a 120% deformation of membranes swollen in H_2O and D_2O. Membranes were wrapped in aluminum foil to ensure that they remain fully hydrated during the measurements. The scattering patterns for the nonstretched membrane were integrated over all directions (isotropic scattering pattern) to obtain 1D scattering curves, representative of the scattering features. For the stretched membranes, the integration was performed along the parallel and perpendicular directions to the SD, to analyze the orthogonal structural effects of the stretching within the membrane.

SAXS Experiments. SAXS patterns were recorded on the ID2 beamline at the ESRF.[36] The wavelength, λ, of the X-ray beam was 1 Å. The detector, located at 1.5 and 8 m from the sample, was an image intensified FReLoN CCD system. Data treatment followed the standard procedures for transmission, flat field, and distortion corrections.

The spectra are extracted from the 2D scattering pattern regrouped by sector and centered to different azymuthal angles, in order to analyze the anisotropy of the structure under stretching. The relative intensity of the scattering is preserved, since the spectra are normalized by the membrane thickness at all deformation extents. For more details about the experimental setup refer to ref 12. Micro-SAXS patterns were recorded on the ID13 beamline at the ESRF. The wavelength of the micro X-ray beam was 0.975 Å, and its dimension was about 10 μm. The detector was located at 49.1 cm from the sample and had a pixel dimensions of 64.45×64.45 μm^2. For SAXS and SANS experiments, the scattering geometry corresponded to a beam perpendicular to the membrane surface and probing the polymeric structure in the meridian plane, MP_1 as depicted in Figure 1a. For Micro-SAXS studies, the sample was prepared and mounted in order to probe both the meridian plane, MP_2, and the equatorial plane, EP.

3. Results

Micro-SAXS in Meridian and Equatorial Planes. A micro X-ray beam of about 10 μm^2 was used to measure the scattering patterns through the thickness of a Nafion 125 membrane. A spectrum measured in the meridian plane, MP_2, through the thickness is shown in Figure 1b; this spectrum is strongly anisotropic, similarly to those typically observed through the membrane plane, MP_1, for stretched Nafion membranes.[12,22−26,31] On the other hand, the spectrum measured in the equatorial plane, EP, remains isotropic after deformation (see Figure 1c). Londono et al. have already reported a similar result using a stack of drawn Nafion membranes.[22] This observation is evidence of the uniaxiality of the deformation process of the Nafion membrane, which was already observed by birefringence measurements for moderate elongation extent.[34] Then the response measured by birefringence becomes biaxial for large elongation extent.

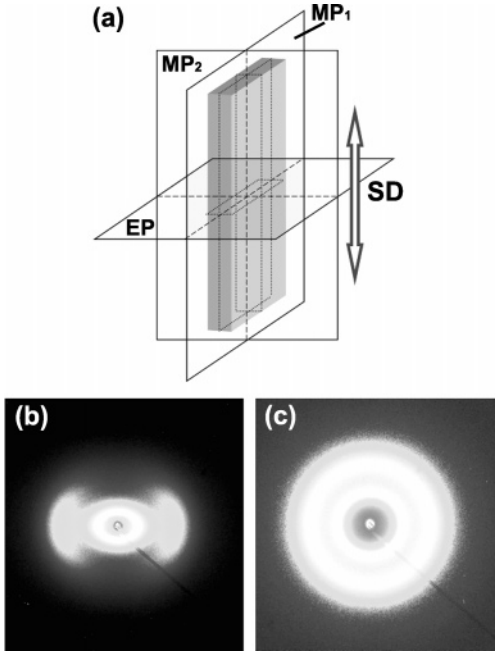

Figure 1. (a) Geometry used to describe the membrane deformation. SD is the stretching direction. EP is the equatorial plane relative to the SD. MP_1 and MP_2 are two major meridian planes. (b and c) Micro-SAXS 2D scattering patterns measured through the thickness of the membrane in the meridian plane MP_2 (b), the incident beam being perpendicular to SD and in the equatorial plane EP (c), and the incident beam being parallel to SD.

SANS and Contrast Variation Experiment. Contrast variation small angle neutron scattering experiments were performed to determine the shape of the scattering objects in drawn and swollen membranes. The procedure to treat SANS data was already used for undrawn Nafion in previous papers,[8,10,31] assuming that in a narrow q-range around the ionomer peak, the scattering intensity can be depicted by a product of a structure and a form factor.[8,10] Then, dividing the spectra measured on a membrane swollen in D_2O by the one measured on the same membrane swollen in H_2O leads to the cancelation of the structure factor, which is not dependent on the solvent scattering length density. The result is then a ratio of two form factors, which was possible to simulate with a simple model based on cylindrical scattering objects. For more details on the division procedure refer to the articles of refs 8 and 10. The experimental division curves normalized by the mean intensity value measured along the SD are presented in Figure 2a.

The general shape of the division curve determined along the SD perpendicular direction after deformation is similar to the one measured before deformation. The minimum at 0.14 Å^{-1} visible on those two curves reveals that the scattering length density profile of the scattering object remains the same, i.e.,

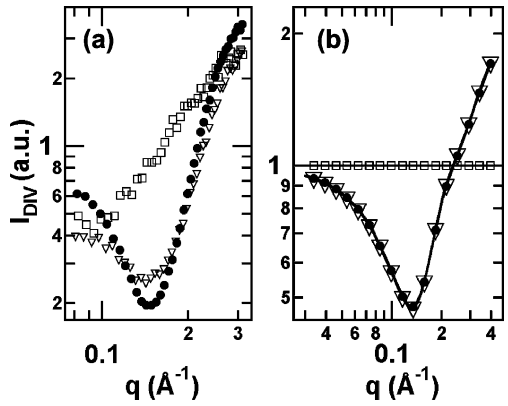

Figure 2. (a) Experimental division curves obtained by dividing the scattering spectra measured from a membrane swollen in D_2O by that measured from the same membrane swollen in H_2O. The ● correspond to the undrawn membrane, □ and ▽ markers represent the data measured parallel and perpendicular to the SD in the MP_1, respectively, after a 120% deformation. (b) Theoretical division curves where the ● correspond to randomly oriented cylinder, □ and ▽ markers represent calculated curves along the directions parallel and perpendicular, respectively, to the cylinder axis. □ and ▽ marker curves collapse on this graph.

the size of those objects remains the same before and after drawing. On the other hand, along the SD direction the minimum at 0.14 Å^{-1} has disappeared, which reveals that after deformation there is no longer variation of the scattering length density along the drawing axis.

SAXS in Meridian Plane. Parts a and b of Figure 3 present the scattering curves from the meridian plane, MP_1, for various deformations after regrouping the 2D data along both major directions: parallel and perpendicular to the SD. The scattering in the two directions evolve in an opposite manners. The intensity and the *q*-position of the ionomer peak decrease with the deformation in the direction parallel to the SD (a) and increase with deformation along the perpendicular direction (b). At smaller angles, the *q*-position of the so-called matrix knee, related to the scattering length density variation between crystalline and amorphous domains in the material,[6,10,31] evolves like the ionomer peak. However, an accurate evaluation of its position and intensity is not easy since the power-law underneath evolves dramatically with the deformation. As shown in Figure 3b, this power-law remains close to q^{-1}, in average, before and after the drawing process along the SD perpendicular direction. However, whereas along the parallel direction the power-law drops; the slope at small angle tends to scale with a q^{-2} regime for large deformation. This trend is more obvious in Figure 4 where the spectra are collected on a Nafion membrane swollen in methanol. The advantage of this treatment is the attenuation of the matrix knee which leads to a more accurate observation of the power-law. The other advantage is that the membrane also tolerates a larger deformation extent before rupture, up to 200%.

4. Discussion

4.1. SANS Contrast Variation Experiment. SANS results show that the intraparticle correlation is lost along the SD, in the *q*-range 0.08−0.3 Å^{-1} (Figure 2a). In contrast, perpendicular to the SD this intraparticle correlation remains similar to those determined from the nondrawn curves. As it was demonstrated previously, the position of the minimum in these division curves is related to the cross-section of the scattering objects,[10,31] which means that the scattering objects are not deformed during the drawing process. Those observations are fully consistent with an orientation of elongated objects along the deformation axis and do not support a deformation of spherical micelles into oblate ellipsoid micelles. To support this assertion, theoretical division curves have been calculated assuming perfectly oriented cylinder-like scattering objects. Such a perfect orientation is nevertheless not the case experimentally, but this is a simple way to give an insight. Figure 2b presents the calculated curves using a core−shell cylinder form factor (see Appendix A). The cylinder length is 500 Å, the core radius is 20 Å with a polydispersity of 30%, and the shell thickness is 5 Å.[10,31] The scattering length density (SLD) of the fluorinated polymeric core is 4.9×10^{10} cm^{-2}.[10,31] The hydrated ionic shell and surrounding solvent SLD are, respectively, -0.61 and -0.53×10^{10} cm^{-2} when solvent is H_2O and 4 and 6.39×10^{10} cm^{-2} when D_2O is used.[10,31] The curves are normalized by the mean intensity value calculated along the SD. The theoretical calculation shows the same trend as the experimental data. After a perfect alignment, the correlation is lost along the SD, while the curve calculated along the SD perpendicular axis is identical to the one of the unaligned system. The slope observed on the experimental data along the SD is most probably the result of poor neutron statistics and the difficulty in a perfect background subtraction, which are due to difficult experimental conditions. We have indeed used aluminum foil to maintain the hydration around the membranes under stretching, and the thickness of the membranes packing was not well controlled.

4.2. Ionomer Peak and Structure Factor. As already mentioned, the *q*-position of the ionomer peak, q_{peak}, is related to *d*, the mean distance between the polymeric aggregates.[9] At first approximation, the Bragg relationship, $d \approx 2\pi/q_{max}$ can be used. The intensity of the peak, $I_{peak}(q)$ is related to the number of the scattering objects that contributes to the scattering signal in the detector plane.

Deformation Model. To analyze the evolution of the ionomer peak during the stretching process, a basic deformation model is proposed. This structural model is based on the fibrillar Nafion morphology proposed previously. To simplify the approach, the polymeric and elongated aggregates are considered cylindrical and at a larger length scale the bundles are represented by virtual rectangular boxes, inside which the cylinders remain parallel to each other, cf. parts a and b of Figure 5. This is a crude approach since we consider an orientational order of the polymeric aggregates, but this representation allows us to develop a simplified deformation model. It is important to point out that the model does not take into account relaxation or creep processes, which probably occur in the material under a load.

The box containing parallel cylinders mimics the aggregate bundle picture and indeed defines the local orientation order between the aggregates. The number of cylinders per box and the size of the boxes are not parameters of the model. During the entire stretching process, the boxes are deformed according to an affine deformation, keeping their volume constant. The boxes evolve from a cube of dimensions $a_0 = b_0 = c_0$ to rectangular boxes of dimensions $a = b \neq c$. The rectangular boxes present square cross-sections due to the uniaxiality of the deformation, and the long axis *c* is along the SD. Throughout the box deformation, the cylinders are tilted preferably toward the SD but remain ordered and parallel to one side of the box. Before deformation, in each box, the cylinders are organized into a square lattice of dimension d_0, cf. Figure 5c. After deformation, the cylinders are localized on a rectangular lattice of dimensions d_{eq} and d_{me}, corresponding, respectively, to the dimensions in the equatorial and meridian sections, as shown in Figure 5d. The intensity and the *q*-position of the first-order

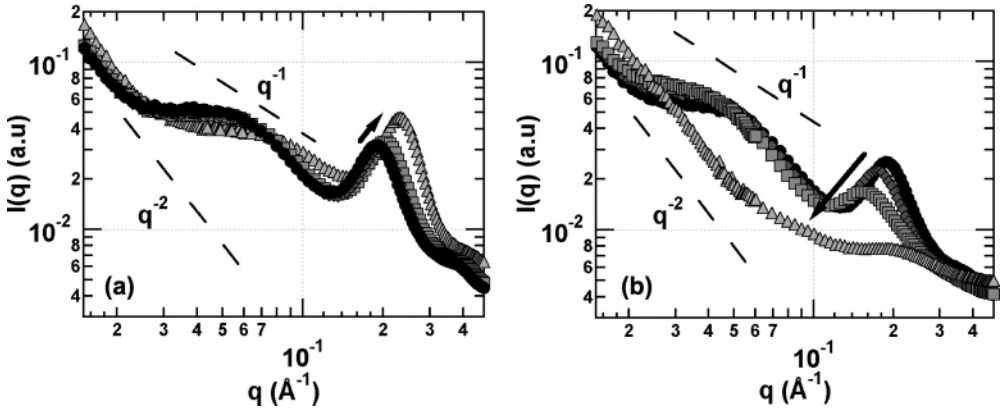

Figure 3. SAXS spectra in the meridian plane, MP_1, parallel to the SD (a) and perpendicular to the SD (b), as a function of the membrane deformation. Four different drawing ratios are presented 0% (●), 7% (♦), 20% (■), and 120% (▲). Black arrows show the ionomer peak evolution with increasing elongation. On both graphics, the dotted lines represent q^{-1} and q^{-2} slopes and are guides for the eyes.

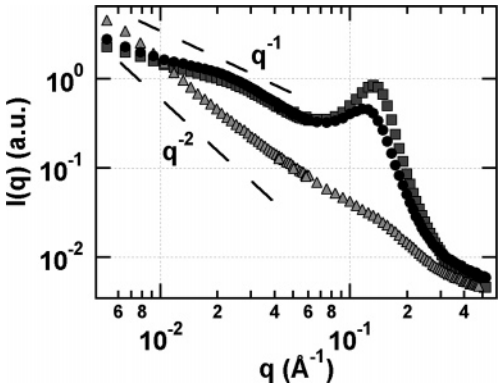

Figure 4. SAXS spectra measured in the meridian plane, MP_1, on a membrane swollen in methanol before deformation (●) and after a 200% deformation along the SD perpendicular (■) and parallel (▲) directions. The dotted lines represent q^{-1} and q^{-2} slopes, as indicated.

peak of the structure factor, respectively, I_{peak} and q_{peak}, are calculated from d_{eq} and d_{me}. I_{peak} and q_{peak} are functions of the angle β on the detector plane and the deformation parameter ϵ, cf. Figure 6. ϵ is defined as the ratio between the box dimension along the deformation axis before and after stretching,

$$\epsilon = c_0/c \tag{1}$$

If the boxes and the whole material are deformed identically then ϵ and λ_{def} are related by

$$\lambda_{def} = \epsilon^{-1} - 1 \tag{2}$$

Details of the model and calculations are developed in Appendix B. The SAXS 2D spectra measured on a membrane drawn at 0, 2, 7, 10, 50, and 70% are presented in Figure 7. The intensity follows a gray scale, where lighter gray corresponds to lower intensity and darker gray to higher intensity. The large and dark corona represents the experimental ionomer peak position. I_{peak} and q_{peak} are calculated through expression 2 using ϵ calculated from the real membranes' deformation. The theoretical results are added on top of the experimental spectra. The calculation leads to ϵ values of, respectively, 1, 0.98, 0.935, 0.909, 0.666, and 0.588. The position of the solid line corresponds to the ionomer peak position, and the size and the darkness of it are related to the intensity. The larger and the darker is the line, the larger is the intensity. It is important to point out that the only adjustable parameter of our model is the initial q value which is set on the nondrawn membrane spectrum and remains constant for all deformations.

As shown in Figure 8a,b, there is a good agreement between experiment and simulation but the consistency in intensity is only qualitative. Our basic model can predict the general evolution of the intensity for all azimuthal angles as a function of the deformation extent. Note that the experimental curve measured on a nonstretched membrane presents a relatively low anisotropy due to membrane processing by extrusion. The fact that the predicted intensity at $\beta = 0$ is much higher than the experimental data means that the model overevaluates the number of cylinders oriented perpendicular to the SD. This point will be discussed later as a limit of our model. On the other hand, the scaling in q-position is excellent for deformations smaller than 40%, then reduces at large deformations, especially along the SD perpendicular direction. Figure 9 points out this deviation between the experimental points corresponding to the q-position of the ionomer peak versus the theoretical prediction. There is an excellent scaling along the deformation axis between experimental and theoretical results, using expression 2. The drift at large deformation can be explained by the fact that the model does not take into account the steric repulsion of the cylinders and their limited deformation in the nonswollen state. The intensity scattered in the perpendicular direction arises mainly from cylinders oriented along the SD. During the deformation, those cylinders get closer to each other until contact is reached, then another regime than the one predicted should be observed. Figure 9 shows this other regime along the perpendicular direction, starting at point A, where experimental data diverge from the predicted curve. The q-position of this divergence (point A) corresponds in the direct space to 30 Å, which is approximately the value of the cylinder diameter.[9] Between points A and B, as deformation keeps increasing, the correlation distance between cylinders decreases, until rupture of the membrane on point B. After breaking, the membrane relaxes to a q value close to the one at point A. A reasonable explanation for this behavior is that (i) at point A, the cylinders are in contact, (ii) between points A and B, the cylinder diameter is deformed elastically by less than 7%, (iii) at point B, after membrane rupture, the system can relax and return to a state where the cylinders are in contact but are not deformed. The cylinder radius deformation measured here is limited to less than 7% which is considerably smaller than the membrane deformation, 120%. Furthermore, contrary to the SANS experiment performed on swollen membranes, the membranes here are under ambient conditions. It is reasonable to consider that the presence of water between the cylinders delays the cylinder deformation to a large drawing ratio. There are less points measured along the SD's parallel direction because the ionomer

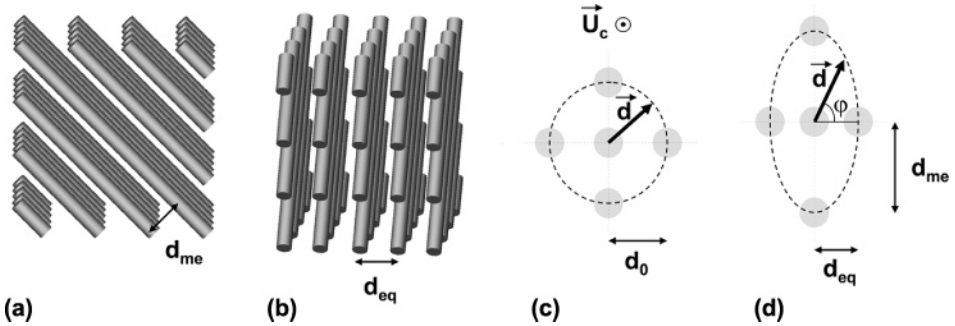

Figure 5. (a and b) Cylinder boxes observed from two different perspectives. (c and d)Cross-sections in the plane perpendicular to the cylinder axis before (c) and after deformation (d). d_{eq} is the distance between cylinders in the equatorial plane, d_{me} is the distance in the meridian plane in which the cylinders are included. The dotted lines in parts c and d represent $d(\varphi)$ which is the distance to the first neighbor considering a liquidlike order.

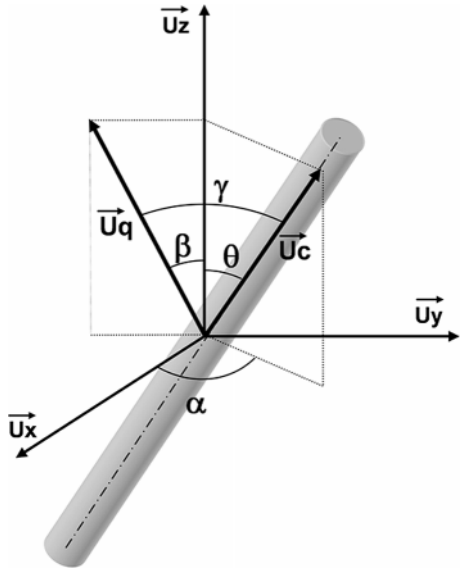

Figure 6. Cylinder in a Cartesian coordinate system ($\mathbf{u_x}$, $\mathbf{u_y}$, $\mathbf{u_z}$) and in a polar coordinate system (α, θ, $\mathbf{u_c}$), The scattering vector, $\mathbf{u_q}$ is included in the detector plane ($\mathbf{u_y}$, $\mathbf{u_z}$) and can be defined by the angles β or γ.

peak disappears in that direction and does not come back after the membrane rupture.

4.3. Power-Law and Form Factor. Calculation of Oriented Cylinders Form Factor. The evolution of the scattering curve at low q underneath the matrix knee can be simulated qualitatively considering an assembly of elongated cylinder-like objects and neglecting any effect of a structure factor in this q-range. The scattering form factor of cylinders is known and can be calculated for different angle distribution profiles, which depend on the deformation of the material.

The intensity scattered by noninteracting cylinders can be expressed as

$$I(q) \propto (F^2(q, \gamma))_\gamma \tag{3}$$

where $F(q, \gamma)$ is the regular expression of the cylinder form factor, given by eq 6 in Appendix A. The previous relation can be rewritten introducing the angles θ, ϕ, and β (Figure 6):[37]

$$I(q) \propto \int_0^{2\pi} \mathrm{d}\alpha \int_0^{2\pi} \sin\theta \, \mathrm{d}\theta p(\theta)[F^2(q, \gamma_+ + F^2(q, \gamma_-)] \tag{4}$$

where $p(\theta)$ is the orientational distribution of the cylinders (see Figure 6) and γ is expressed as

$$\cos\gamma_\pm = \sin\theta \cos\alpha \cos\beta \pm \cos\theta \sin\beta \tag{5}$$

Figure 10 shows the intensities scattered by cylinders along the SD's parallel direction, $\beta = 0$, for three different orientational distributions of the cylinders. The intensities scattered along the perpendicular direction, $\beta = \pi/2$, have been calculated but are not presented on the graphic; they are similar for both orientational distribution to the scattering curve calculated with the flat profile. The cylinders are 30 Å in diameter and a large arbitrary value is chosen for the length, $L = 5000$ Å, in order to avoid oscillations of the curves in the q-range of interest, which would be due to a finite cylinder length value. As a reference we use a spectrum calculated from a uniform orientation distribution, which corresponds to a nondeformed system. In that case, the spectra are identical in the parallel and perpendicular direction. The second orientational distribution used is extracted from the previous deformation model, with $p(\theta) = n(\theta)$, and $\epsilon = 0.333$ corresponding to a 200% deformation. The spectrum in the perpendicular direction is similar to the previous spectra, whereas along the parallel direction, the intensity and the slope at low q of the spectrum decrease. The third angular profile used is empirical and close to the second one but drops down to 0 faster as θ increases, $p(\theta) = \exp(A \cos^2\theta)$, with $A = 10$. In that case, the main characteristics of the spectra are identical to the second one but more pronounced. Along the parallel direction, at small q the spectrum presents a power-law close to q^{-2} which is observed experimentally on highly drawn membranes, as shown in Figure 4. Again, the results lead to the conclusion that our deformation model overevaluates the number of cylinders oriented perpendicular to the SD. In refs 12, 33, and 34, the authors have shown that the deformation of the Nafion membrane involves two mechanisms: (i) rotation of the cylinder bundles at small draw ratios and (ii) orientation of the cylinders within the bundles, which is predominant at large draw ratios. The model that we propose in this paper depicts only the cylinder tilting, considering an affine deformation of the bundles. Adding an extra parameter describing the bundle tilting, involving the cylinder boxes tilting, should definitely improve the prediction.

5. Conclusion

The structure of Nafion membranes under deformation is studied by SAXS and SANS techniques. Microbeam SAXS experiments demonstrate the uniaxiality of the deformation at moderate elongation extent. SANS experiments using the contrast variation method show that the scattering objects are oriented without significant deformation, which is consistent with the elongated polymeric aggregates model and an alignment of the aggregates along the stretching direction. The q-position and intensity of the ionomer peak as a function of the drawing extent were simulated through a basic model based on the

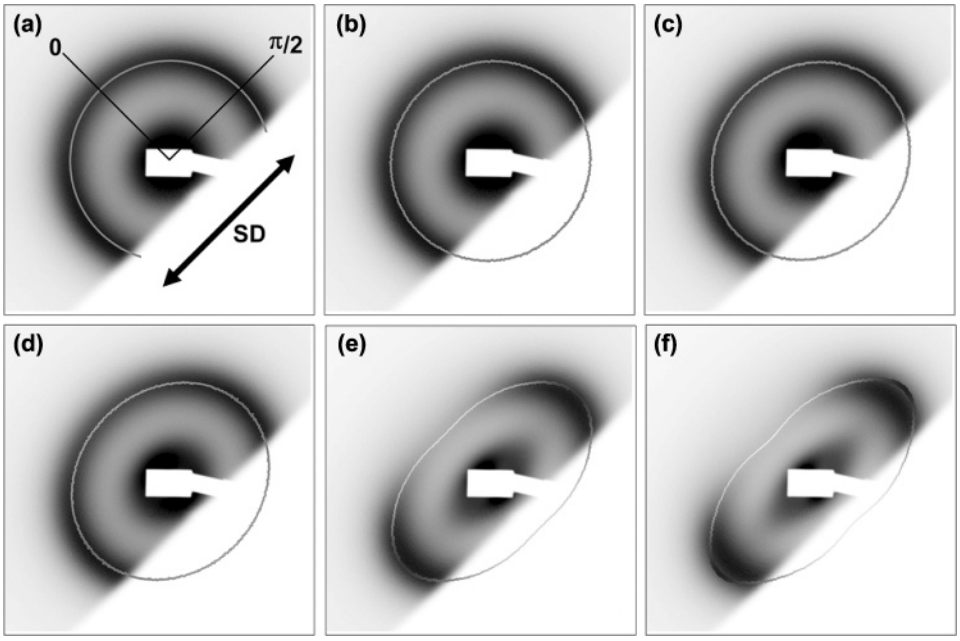

Figure 7. 2D scattering patterns measured in MP_1 as a function of the membrane deformation, λ_{def}, presented in gray scale. λ_{def} are 0% (a), 2% (b), 7% (c), 10% (d), 50% (e), and 70% (f); the correspondingly calculated values for ϵ are, respectively, 1, 0.98, 0.935, 0.909, 0.666, and 0.588. These values were used to calculate ionomer peak position and intensity (represented on top of the spectra through a solid gray line). The size and the darkness of the gray lines are relative to the intensity. The larger and the darker is the line the larger is the intensity. Note that the same scales are used in all spectra. The stretching direction SD and the orientation of the azimuthal angle $\beta = 0$ and $2/\pi$ are given on spectrum a and remain the same for all the other spectra.

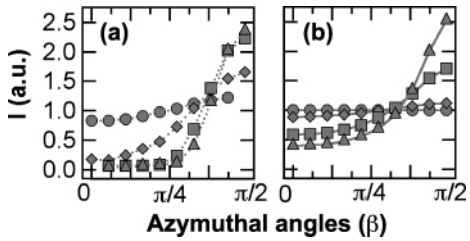

Figure 8. (a) Experimental data extracted from ref 12 Copyright 2004 American Chemical Society and (b) model prediction of the ionomer peak intensities versus the azimuthal angle β as a function of the drawing extent. The deformation values in the graphs (a) are 0% (●), 8% (♦), 43% (■), and 85% (▲) and the respectively calculated values (b) for ϵ are 1 (●), 0.93 (♦), 0.7 (■), and 0.57 (▲). The experimental and theoretical curves are normalized by the average intensity over β before stretching.

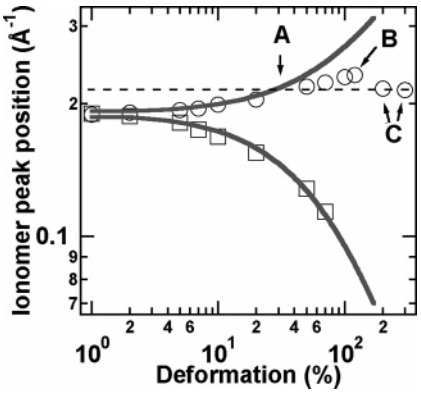

Figure 9. Model prediction (solid lines) versus experimental ionomer peak q-position (markers) along the SD's perpendicular (○) and parallel (□) directions. Points in region C are measured a few seconds after membrane rupture.

orientation of cylinders, with good agreement to the experimental data. The low q power-law was simulated using a cylinder form factor, considering an angular profile distribution

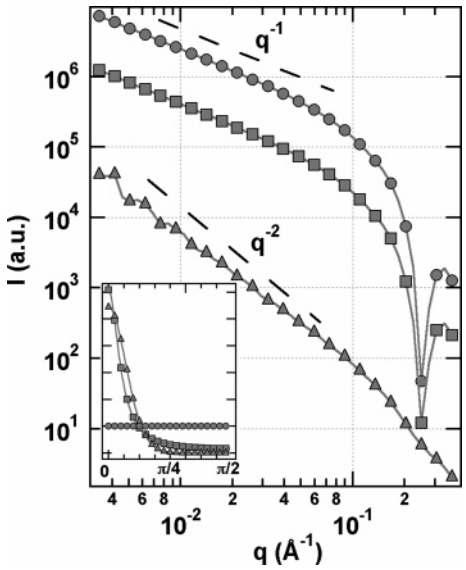

Figure 10. Cylinder form factors calculated along the SD parallel direction for three different orientation distributions shown in the bottom left inset. ● represent the calculation from a flat profile which corresponds to a nonoriented system. ■ represent the result obtained from an orientation distribution extracted from our deformation model, with $p(\theta) = n(\theta)$ and $\epsilon = 0.333$ corresponding to a 200% deformation. ▲ represent the calculation using an empirical orientation distribution, $p(\theta) = \exp(A \cos^2 \theta)$, with $A = 10$.

of the cylinders. All the analysis of our experimental data over a broad range of scattering vectors are consistent with a structure based on fibrils having, at the first order, 35 Å mean diameter.

Acknowledgment. The authors are grateful to the European Synchrotron Radiation Facility (ESRF, Grants ID02 SC-959 and ID13 SC-836) for the beam time allocations and U. Volker and S. Roth as local contacts for the SAXS and micro-SAXS experiments. Thanks also to the Institut Laue Langevin (ILL,

Grant 9-11-886) for providing neutron beam time and I. Grillo as a local contact for her help in completion of the SANS experiments.

6. Appendix A

In this appendix we develop the calculation of the core−shell cylinder form factor taking orientational order into account. The regular expression of cylinder form factor, F, is written as

$$F(q, \gamma) = \Delta\rho V P(q, \gamma, R) = \Delta\rho V \frac{\sin(qL\cos\gamma)}{qL\cos\gamma}\frac{2J_1(qR\sin\gamma)}{qR\sin\gamma} \quad (6)$$

where L and R are half the length and the radius of the cylinder, respectively. q is the norm of the scattering vector, γ is the angle between the cylinder axis $\mathbf{u_c}$ and the scattering vector $\mathbf{u_q}$ (cf. Figure 6), and $\Delta\rho$ and V are the scattering contrast and the cylinder volume, respectively.

The core shell cylinder form factor, F_{cs} is

$$F_{cs}(q, \gamma) = P(q, \gamma, R + s) + \frac{\Delta\rho_2}{\Delta\rho_1}\frac{V(R)}{V(R+s)}P(q, \gamma, R) \quad (7)$$

with $V(r)$ the volume of a cylinder with radius r and length $2L$, $\Delta\rho_1 = \rho_{shell} - \rho_{solvent}$ and $\Delta\rho_2 = \rho_{core} - \rho_{shell}$.

The isotropic intensity corresponding to the membrane before deformation is calculated integrating F_{cs} over all γ, $\langle F_{cs}^2(q, \gamma)\rangle_\gamma$. The intensity scattered by a cylinder along the parallel and perpendicular directions of its axis is given respectively by $F_{cs}^2(q, \gamma = 0)$ and $F_{cs}^2(q, \gamma = \pi/2)$.

7. Appendix B

Here we develop the details of the deformation model. The boxes are depicted by stacks of framed sections containing ordered cylinders, as shown in Figure 5a,b. Those sections are all meridian sections in regards to the deformation axis. During deformation, the sections are deformed from a square frame of dimensions b_0 and c_0 to a rectangular frame of dimensions b and c. In the equatorial plane, the distance between the parallel framed sections evolves from d_0 to d_{eq}. In this model, the cylinders are fixed on the frame, which leads to their tilting during the deformation.

First, the main axis and planes of system shall be introduced, all defined by the vectors $\mathbf{u_x}$, $\mathbf{u_y}$, $\mathbf{u_z}$, $\mathbf{u_c}$, and $\mathbf{u_q}$ (see Figure 6). $\mathbf{u_z}$ corresponds to the stretching axis; $\mathbf{u_x}$ defines the beam axis; the plane defined by the vectors $\mathbf{u_x}$ and $\mathbf{u_y}$ is the equatorial plane; the plane defined by the vectors $\mathbf{u_z}$ and $\mathbf{u_c}$ corresponds to the framed section. $\mathbf{u_q}$ is included in the detector plane defined by the vectors $\mathbf{u_y}$ and $\mathbf{u_z}$.

The direction of the cylinders in each box is given by the unit vector, $\mathbf{u_c}$, which is defined by the angles θ and α, as shown in Figure 6. θ corresponds to the angle between the cylinders and the deformation axis in the meridian sections. α is the angle between the framed sections and the beam axis in the equatorial plane. Note that during the stretching process, α is constant within a box. The vector $\mathbf{u_c}$ is defined as

$$\mathbf{u_c} = \begin{vmatrix} \sin\theta\cos\alpha \\ \sin\theta\sin\alpha \\ \cos\theta \end{vmatrix} \quad (8)$$

Assuming an affine deformation of the boxes with a constant box volume $a_0b_0c_0 = abc$ leads to trivial relations of the deformation parameter ϵ to the boxes' dimensions: by definition $\epsilon = c_0/c$ and $a/a_0 = b/b_0 = \epsilon^{-1/2}$.

Calculation of d_{eq} and d_{me}. d_{eq} can be calculated considering the homothetic relation $a/a_0 = d_{eq}/d_0$. Then,

$$d_{eq} = d_0\epsilon^{-1/2} \quad (9)$$

d_{me} can be determined from the initial conditions and the deformation parameter, using θ_0, the angle between the cylinders and the stretching axis before deformation. Considering the homothetic and the regular angular relations in the meridian section leads to

$$d_{me} = d_0\frac{a}{a_0}\frac{\cos\theta}{\cos\theta_0} = d_0\frac{c}{c_0}\frac{\sin\theta}{\sin\theta_0} \quad (10)$$

Both expressions of d_{me} can be combined, obtaining

$$\theta_0 = \arctan[\epsilon^{-3/2}\tan\theta] \quad (11)$$

Equations 9 and 10 are inserted in 11, leading to

$$d_{me} = d_0\epsilon^{-1/2}\frac{\cos\theta}{\cos[\arctan[\epsilon^{-3/2}\tan\theta]]} \quad (12)$$

Simplify the approach, a liquidlike order is considered to determine the position of the first neighbor cylinders, which is represented by the vector $\mathbf{d}$ as shown in Figure 5c,d. The first neighbor cylinders are preferably located on a circle of radius d_0 before stretching and on an ellipse of radii d_{eq} and d_{me} after stretching. The ellipse radius $d(\varphi)$ is the distance between cylinders as a function of φ, the angle between d_{eq} and $\mathbf{d}$ in the ellipse section (orthogonal to the cylinders). $d(\varphi)$ can be then expressed as

$$d(\varphi) = \frac{d_{me}d_{eq}}{[d_{me}^2\cos^2\varphi + d_{eq}^2[1 - \cos^2\varphi]]^{1/2}} \quad (13)$$

The scattering vector $\mathbf{q}$ resulting from the correlation distance, represented by the vector $\mathbf{d}$, can be approximated using the Bragg relation

$$\mathbf{q} \approx \frac{2\pi}{d^2}\mathbf{d} \quad (14)$$

Note that $|\mathbf{q}|$ corresponds to q_{peak}, which is the q-position of the first-order peak of the structure factor. $\mathbf{q}$ is in the ellipse section then orthogonal to $\mathbf{u_c}$. Furthermore, $\mathbf{q}$ has to be in the detector plane in order to be measured. So $\mathbf{u_q}$, the unit vector collinear to the scattering vector $\mathbf{q}$, is expressed as

$$\mathbf{u_q} = [\cos^2\theta + \sin^2\theta\sin^2\alpha]^{-1/2}\begin{vmatrix} 0 \\ -\cos\theta \\ \sin\theta\sin\alpha \end{vmatrix} \quad (15)$$

In the detector plane defined by both vectors $\mathbf{u_y}$ and $\mathbf{u_z}$, the vector $\mathbf{u_q}$ has a simpler expression

$$\mathbf{u_q} = \begin{vmatrix} 0 \\ \sin\beta \\ \cos\beta \end{vmatrix} \quad (16)$$

where β is the angle between the vector $\mathbf{q}$ and the SD on the detector plane (see Figure 6). The combination of eqs 15 and 16 leads to a relation between the angles θ, β, and α

$$\theta = \arctan\left[\frac{-1}{\tan\beta\sin\alpha}\right] \quad (17)$$

Considering the scalar product of $\mathbf{u_q}$ and $\mathbf{u_{eq}}$, with $\mathbf{u_{eq}}$ the unit vector parallel to d_{eq} leads to

$$\cos\varphi = \frac{\cos\alpha\cos\beta}{[\cos^2\theta + \sin^2\theta\sin^2\alpha]^{1/2}} \tag{18}$$

since

$$\mathbf{u_{eq}} = \begin{vmatrix} \sin\alpha \\ -\cos\alpha \\ 0 \end{vmatrix} \tag{19}$$

The combination of the relationships in eqs 13 and 14 leads to an approximation of the q_{peak} (q-position of the first order of the structure factor)

$$q_{peak} \approx 2\pi \frac{[{d_{me}}^2\cos^2\varphi + {d_{eq}}^2[1-\cos^2\varphi]]^{1/2}}{d_{me}d_{eq}} \tag{20}$$

Inserting expressions in eqs 9, 12, 17, and 18 in the previous expression leads to an approximation of $q_{peak}(\epsilon, \alpha, \beta)$ dependent only on variables ϵ, α, and β.

The distribution of cylinders as a function of their orientation θ can be expressed as

$$n(\theta) \propto \frac{d\theta_0}{d\theta} = \left[\epsilon^{3/2}\left[\cos^2\theta + \frac{\sin^2\theta}{\epsilon^3}\right]\right]^{-1} \tag{21}$$

Introducing eq 17 in the previous relation leads to the distribution $n(\epsilon, \alpha, \beta)$ only as a function of the three variables. Finally, integrating $q_{peak}(\epsilon, \alpha, \beta)$ and $n(\epsilon, \alpha, \beta)$ over $\sin(\alpha)\,d\alpha$, for α between 0 and 2π, leads to the expressions of $q_{peak}(\epsilon, \beta)$ and $I_{peak}(\epsilon, \beta)$, which are the q-position and the relative intensity of the first-order peak scattered by many cylinder boxes presenting various initial orientations:

$$q_{peak}(\epsilon, \beta) \approx \frac{\int_0^{2\pi} n(\epsilon, \alpha, \beta) q_{peak}(\epsilon, \alpha, \beta)\sin\alpha\,d\alpha}{\int_0^{2\pi} n(\epsilon, \alpha, \beta)\sin\alpha\,d\alpha} \tag{22}$$

and

$$I_{peak}(\epsilon, \beta) \propto \int_0^{2\pi} n(\epsilon, \alpha, \beta)\sin\alpha\,d\alpha \tag{23}$$

References and Notes

(1) Schlick, S. *Ionomers, Characterization, Theory and Applications*; CRS Press: Boca Raton, FL, 1995.
(2) Heitner-Wirguin, C. *J. Membr. Sci.* **1996**, *120*, 1−33.
(3) Tant, M. R.; Mauritz, K. A.; Wilkes, G. L. *Ionomers. Synthesis Structure, Properties and Applications*; Blackie Academic & Professional: London, U.K., 1997.
(4) Mauritz, K. A.; Moore, R. B. *Chem. Rev.* **2004**, *104*, 4535−4585.
(5) Loppinet, B.; Gebel, G.; Williams, C. *J. Phys. Chem. B* **1997**, *101*, 1884−1892.
(6) Gierke, T. D.; Munn, G. E.; Wilson, F. C. *J. Polym. Sci., Polym. Phys.* **1981**, *19*, 1687−1704.
(7) Gebel, G. *Polymer* **2000**, *41*, 5829−5838.
(8) Rollet, A.-L.; Diat, O.; Gebel, G. *J. Phys. Chem. B* **2002**, *106*, 3033−3036.
(9) Rubatat, L.; Rollet, A.-L.; Gebel, G.; Diat, O. *Macromolecules* **2002**, *35*, 4050−4055.
(10) Rubatat, L.; Gebel, G.; Diat, O. *Macromolecules* **2004**, *37*, 7772−7783.
(11) Starkweather, H. W. *Macromolecules* **198**2, *15*, 320−323.
(12) van der Heijden, P. C.; Rubatat, L.; Diat, O. *Macromolecules* **2004**, *37*, 5327−5336.
(13) Lehmani, A. A.; Durand-Vidal, S.; Turq, P. *J. Appl. Polym. Sci.* **1998**, *68*, 503−508.
(14) James, P. J.; Antognozzi, M.; Tamayo, J. J.; McMaster, T. J.; Newton, J. M.; Miles, M. J. *Langmuir* **2001**, *17*, 349−360.
(15) Gebel, G.; Lambard, J. *Macromolecules* **1997**, *30*, 7914−7920.
(16) Grot, W. G. *Macromolecules* **2006**, *39*, 4772−4778.
(17) Gebel, G.; Diat, O. *Fuel Cells* **2005**, *5*, 261−276.
(18) Lin, H.-L.; Yu, T. L.; Han, F.-H. *J. Polym. Res.* **2006**, *13*, 379−385.
(19) Lin, J.; Wycisk, R.; Pintauro, P. N.; Kellner, M. *Electrochem. Solid State Lett.* **2007**, *10*, 19−22.
(20) Kyu, T.; Hashiyama, M.; Eisenberg, A. *Can. J. Chem.* **1983**, *61*, 680−687.
(21) Almeida, S. H.; Kawano, Y. *J. Therm. Anal. Calorim.* **1999**, *58*, 569−577.
(22) Londono, J. D.; Davidson, R. V.; Mazusr, S. *Polym. Mater. Sci. Eng.* **2001**, *85*, 23−24.
(23) Cable, K. M.; Mauritz, K. A.; Moore R. B. *Polym. Prepr. (Am. Chem. Soc., Div. Polym. Chem.)* **1994**, *35*, 421−422.
(24) Fujimura, M.; Hashimoto, T.; Kawai, H. *Macromolecules* **1982**, *15*, 136−144.
(25) Elliott, J. A.; Hanna, S.; Elliott, A. M. S.; Cooley, G. E. *Macromolecules* **2000**, *33*, 4161−4171.
(26) Landis, F. A.; Moore, R. B.; Page, K. A.; Han, C. C. *Polym. Mater. Sci. Eng.* **2002**, *87*, 121−122.
(27) Yeo, S. C.; Eisenberg, A. *J. Appl. Polym. Sci.* **1977**, *21* (4), 875−898.
(28) Hodge, I. M.; Eisenberg, A. *Macromolecules* **1978**, *11* (2), 289−293.
(29) Miura, Y.; Yoshida, H. *Thermochim. Acta* **1990**, *163*, 161−168.
(30) Page, K. A.; Cable, K. M.; Moore, R. B. *Macromolecules* **2005**, *38* (15), 6472−6484.
(31) Rubatat, L. Thesis in Physics, Université Joseph Fourier, Grenoble, France, 2003.
(32) Liu, D.; Hickner, M. A.; Case, S. W.; Lesko, J. J. *J. Eng. Mater. Technol. Trans. ASME* **2006**, *128* (4), 503−508.
(33) van der Heijden, P. C.; de la Rosa, A.; Gebel, G.; Diat, O. *Polym. Adv. Technol.* **2005**, *16*, 102−107.
(34) van der Heijden, P. C.; Diat, O. *Nucl. Instrum. Methods Phys. Res., Sect. B* **2005**, *238*, 43−49.
(35) van der Heijden, P. C.; Bouzenad, F.; Diat O. *J. Polym. Sci., Part B: Polym. Phys.* **2004**, *42* (15), 2857−2870.
(36) Urban, V.; Panine, P.; Ponchut, C.; Boesecke, P.; Narayanan, T. *J. Appl. Crystallogr.* **2003**, *36*, 809−811.
(37) Hayter, J. B.; Penfold, J. *J. Phys. Chem.* **1984**, *88*, 4589−4593.

MA070362S